

Particle Dynamics and Rapid Trapping in Electro-Osmotic Flow Around a Sharp Microchannel Corner

Matan Zehavi and Gilad Yossifon

*Faculty of Mechanical Engineering, Micro and Nanofluidics Laboratory,
Technion–Israel Institute of Technology, Technion City 32000, Israel and*

**Corresponding author: yossifon@tx.technion.ac.il*

Abstract

We study here the curious particle dynamics resulting from electro-osmotic flow around a microchannel junction corner whose dielectric walls are weakly polarizable. The hydrodynamic velocity field is obtained via superposition of a linear irrotational term associated with the equilibrium zeta potentials of both the microchannel and particle surfaces and the non-linear induced-charge electro-osmotic flow which originates from the interaction of the externally applied electric field on the charge cloud it induces at the solid-liquid interface. The particle dynamics are analyzed by considering dielectrophoretic forces via the addition of a mobility term to the flow field in the limit of Stokes drag law. The former, non-divergence free term is responsible for migration of particles towards the sharp microchannel junction corner, where they can potentially accumulate. Experimental observations of particle trapping for various applied electric fields and microparticle size are rationalized in terms of the growing relative importance of the dielectrophoretic force and induced-charge contributions to the global velocity field with increasing intensity of the externally applied electric field.

I. INTRODUCTION

The present contribution focuses on the dynamics of particles and their accumulation in electro-osmotic flow through micro-channel junctions which are a basic element of microfluidic systems. This work thus extends previous studies [1–4] that focused on describing the interesting hydrodynamic behavior, wherein beyond a critical level of external-field intensity, vortices are observed to appear within the flow around (sharp) corners of micro-channel junctions. The generation of such vortices is potentially useful in certain applications as a means to enhance and control micro-fluid mixing [5–7]. In other situations the appearance of vortices may need to be suppressed so as to avoid accumulation of suspended particles leading to the eventual jamming of the device [2]. In linear electro-osmosis, when the equilibrium zeta potential is uniform and independent of the external field, the resulting flow is irrotational. However, the small yet finite polarizability of the walls gives rise to an additional, non-linear, electro-kinetic mechanism termed induced-charge electro-osmosis (ICEO) [8]. When an external field is applied to the system, it sets off within the electrolyte solution transient Ohmic currents which create a non-uniform charge cloud near the walls. Thus, a non-uniform distribution of induced zeta potential is established whose magnitude is proportional to the external-field intensity. The Helmholtz-Smoluchowski slip velocity at the fluid-solid interface resulting from the interaction of the electric field and the induced-charge cloud is non-linear in the applied field and generates an electro-osmotic flow which is not necessarily irrotational.

Thamida & Chang [2] pointed out that the above mechanism produces opposite polarization of the respective upstream and down-stream faces of the corner. Furthermore, for a sufficiently strong external field this ICEO not only dominates the local flow near the corner but produces downstream macro-scale vortices as well [3]. Thamida & Chang [2] also observed that an interesting colloid accumulation occurs at the corner, however no attempt was made to address this particle trapping mechanism either theoretically or experimentally.

As will be shown herein, the rapid trapping occurs due to a combination of the short range DEP trapping force and the long-range induced electro-osmotic flow which feeds the particles. Previous studies have examined particle trapping and separation based on insulator-based dielectrophoresis (iDEP) using sharp tips among other geometries [9–11]. However, in contrast to the current study, these works have treated such structures as insulators and

as a result induced electrokinetic effects, emanating from the finite but small dielectric polarizability of the wall materials, were overlooked. Nevertheless, efficient trapping via the combination of a short range DEP force and far-field hydrodynamics has been shown for a variety of flow generation mechanisms. AC electroosmosis (ACEO), which uses electrodes embedded within the microchannel, has attracted a lot of attention as means for vortex generation and particle trapping through hydrodynamic forces that focus the particles into the stagnation point of the vortices [12–15]. Additionally, similar accumulation has recently been demonstrated [16] at the stagnation points of electro-osmotic vortices of the second kind formed at the interface of a microchannel and a wide nanoslot.

It is thus the focus of the current study to provide for the first time a thorough explanation, based on both theory and experiments, for the rapid particle trapping due to the combined forces of the DEP and ICEO vortex at the corner of a microchannel. In the following, we describe the experimental methods in sec. 2, the theoretical model in sec. 3, the results and discussion in sec. 4 and concluding comments in sec. 5.

II. EXPERIMENTAL METHODS

A. Fabrication of the device

A L-junction microchannel connected to two reservoirs at opposite ends (Fig. 1(a)) with a depth (normal to the plane of view) of 120 μm was fabricated from PDMS (Polydimethylsiloxane, Dow-corning Sylgard 184) using a rapid prototype technique [17]. We used a high resolution (3 μm) chrome mask for the creation of the master. The radii of curvature of the corner is estimated to be $\sim 6 \mu\text{m}$. The channel was then sealed by a PDMS coated (30 μm thick) microscope glass slide, using a plasma bonding process [18]. Two large (19 mm diameter) reservoirs were inserted into the PDMS inlets so as to minimize possible pressure driven flow due to induced pressure head and to allow the introduction of Platinum wire electrodes (Fig. (1)b).

B. Experimental setup

A high voltage DC power supply (Stanford Research Systems PS350) was connected to the platinum wire electrodes (0.5 mm platinum wire, Sigma-Aldrich). An electrolyte solution of

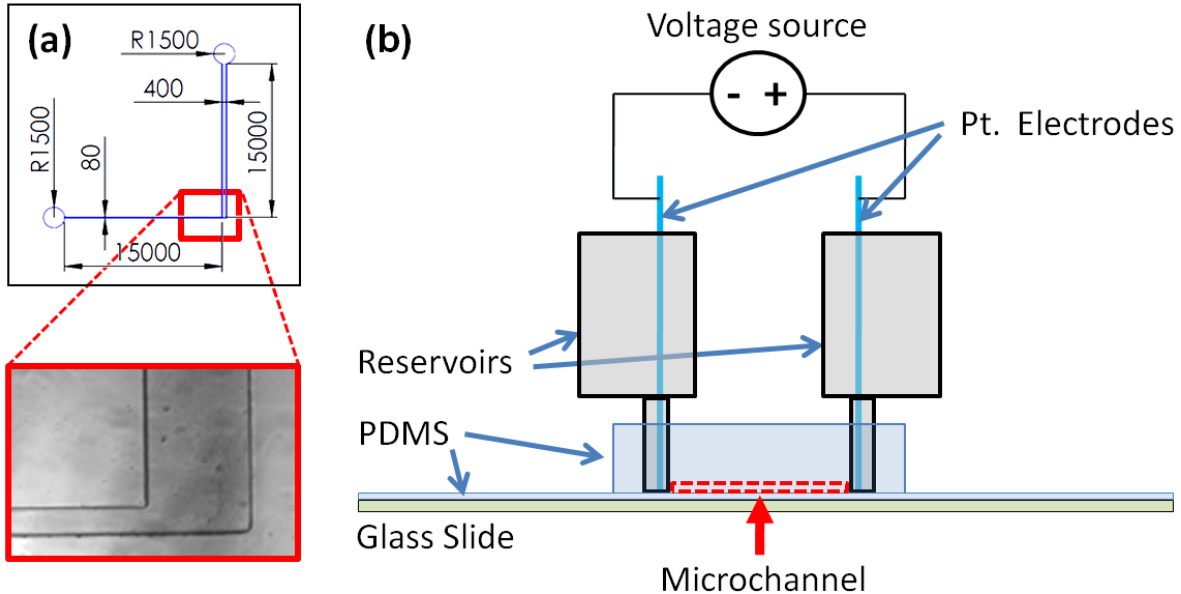


Figure 1: (a) Schematics of the L-junction microchannel device along with a microscope image of the junction region and (b) the experimental flow system setup. Dimensions are in μm .

$10^{-5}[\text{M}]$ Potassium Chloride (conductivity $\sigma_f = 2 \mu\text{S}/\text{cm}$) was seeded by negatively charged fluorescently tagged tracer particles (Fluoro-Max, Thermo-Scientific) of various sizes (0.48, 1 and 2 μm) and volumetric concentrations of (0.0025%, 0.01%, 0.04% respectively). The particles were visualized dynamically using a spinning disc confocal system (Yokogawa CSU-X1) connected to a camera (Andor iXon3) and installed on an inverted microscope (Nikon TI Eclipse). Prior to the sudden application of the external field the system was equilibrated to minimize initial pressure driven flow.

III. THEORETICAL MODEL

A. Electrostatics and hydrodynamics

Here we extend the theoretical analysis of Yossifon et al. [3] for ICEO around a sharp corner to include DEP forces acting on particles. For brevity, in deriving the latter hydrodynamic contribution to the particle motion we will closely follow their derivation, skipping the details and showing only the main results. The current problem for the L-junction differs from that of the T-junction microchannel configuration of Yossifon et Al. 2006 [3] only in

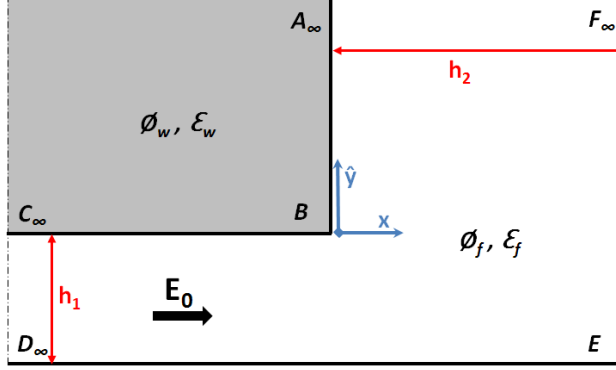


Figure 2: The L-junction configuration

that the mid-narrow channel symmetry line is replaced by a wall (i.e. we apply an electroosmotic slip velocity instead of a symmetry condition at $D_\infty E$ boundary, see Fig. 2). It is noted that for a low-conductivity electrolyte, electrothermal effects stemming from Joule heating (which scales linearly with the conductivity) become minimal [19]. Moreover, for the current geometry, it may also be shown that any inplane temperature gradients (which would potentially control the 2D electrothermal forcing) resulting from such minimal Joule heating, would be negligible as most of the generated heat dissipate through the bottom slide which has minimum thermal resistance. The introduction into the problem of a small but finite wall dielectric constant ϵ_w , necessitates the simultaneous calculation of both ϕ_f and ϕ_w , the electrostatic potentials within the fluid and wall domains, respectively. On the microscale of the electric double layer these potentials are coupled through the boundary conditions imposing continuity of the potential and specifying the jump in electric displacement across the true solid-liquid interface [20]. The thin-double-layer approximation was previously extended by Yossifon et al. 2006 [3] to account for the electric-field leakage through the wall for an arbitrary value of the dielectric constants ratio ϵ_w/ϵ_f , to obtain an appropriate macro scale boundary condition for a symmetric electrolyte solution relating ϕ_f just outside the double layer and ϕ_w at the surface of the wall

$$\phi_w + \alpha \frac{\partial \phi_w}{\partial n} = \phi_f + \zeta^{eq} \text{ on } A_\infty B C_\infty. \quad (1)$$

The dimensionless Robin-type boundary condition (1) is formulated in terms of the dimensionless electric potentials ϕ_f , ϕ_w and the equilibrium zeta-potential ζ^{eq} normalized by $E_0 h_1$, wherein h_1 is the width of the narrow channel and E_0 is the magnitude of the externally

applied electric field within the narrow channel far from the junction. Here $\frac{\partial}{\partial n}$ denotes the derivative in the direction normal to the wall pointing into the fluid domain. Appearing in (1) is the parameter $\alpha = \frac{\epsilon_w}{\epsilon_f}(\kappa h_1)^{-1}$, wherein κ^{-1} is the (presumed small) Debye length, which represents the thickness of the electric double layer. Under this macro scale boundary condition (1) the dimensionless electric potentials within the bulk fluid and within the wall both satisfy the Laplace equation. In addition, the potential within the bulk fluid satisfies the Neumann-type boundary condition $\frac{\partial \phi_f}{\partial n} = 0$ applied on the channel walls ($A_\infty BC_\infty$ and $D_\infty EF_\infty$ in Fig. 2). These boundary conditions are supplemented by the requirements that $\frac{\partial \phi_f}{\partial x} = -1$ within the narrow channel far from the junction ($x \rightarrow -\infty$) (see Fig. 2) and by conservation of electric-field flux $\frac{\partial \phi_f}{\partial y} = -\frac{h_1}{h_2}$ far from the junction within the wider channel ($y \rightarrow \infty$), as well as appropriate 'far field' ($x^2 + y^2 \rightarrow \infty$) decay conditions within the wall domain.

The problems governing ϕ_f and ϕ_w are thus decoupled and may be solved recursively. Making use of the Schwartz-Christoffel (e.g. Milne-Thomson [21]) transformation

$$z(t) = \frac{1}{\pi} \left[\frac{h_2}{h_1} \ln \left(\frac{t+1}{t-1} \right) + 2 \tan^{-1} \left(\frac{h_1}{h_2} t \right) - \pi \right], \quad (2)$$

and

$$\omega(t) = \frac{1 + (h_1/h_2)^2}{1 - t^2}. \quad (3)$$

the physical complex $z = x + iy$ plane is mapped onto the upper half of the $\omega = \xi + i\eta$ plane, to obtain for a 2D potential of a point charge located at $\omega = 1$

$$\phi_f = \frac{1}{\pi} \text{Re} \{ \ln(\omega - 1) \}, \quad (4)$$

wherein ' $\text{Re} \{ \}$ ' denotes the real part. Expanding (2,3) and (4) for $|\omega| \ll 1$ (corresponding to $|t| \gg \frac{h_2}{h_1}$) one obtains the following potential function:

$$\phi_f \sim \frac{1}{\pi} \left(1 + \left(\frac{h_1}{h_2} \right)^2 \right)^{1/3} \text{Re} \left\{ \left(-\frac{3\pi}{2} z \right)^{2/3} \right\}, \quad (5)$$

which holds in the vicinity of the corner $z = 0$. Once ϕ_f is known, one can calculate ϕ_w to satisfy Laplace's equation within the wall domain and (1) from which we find the total zeta potential to be

$$\zeta = \phi_w - \phi_f = \zeta^{eq} + \zeta^i \text{ on } A_\infty BC_\infty, \quad (6)$$

wherein $\zeta^i = -\alpha \frac{\partial \phi_w}{\partial n}$ denotes the induced zeta potential. On the channel walls ($D_\infty EF_\infty$) opposite from those forming the corner ($A_\infty BC_\infty$) the latter effect is negligible and it is assumed that $\zeta = \zeta_w^{eq}$.

The fluid velocity \mathbf{v} and pressure p are normalized by $\varepsilon_0 \varepsilon_f E_0^2 h_1 / \eta$ and $\varepsilon_0 \varepsilon_f E_0^2$, respectively, where η denotes the dynamic viscosity of the electrolyte solution and ε_0 is the permittivity of vacuum. The quasi-steady, small-Reynolds number flow of the bulk electro-neutral fluid is governed by the continuity equation $\nabla \cdot \mathbf{v} = 0$ and the Stokes equation $\nabla p = \nabla^2 \mathbf{v}$. On the channel walls ($A_\infty BC_\infty$ and $D_\infty EF_\infty$ in Fig. 2) \mathbf{v} satisfies the vanishing of the fluid velocity normal to the wall and the Helmholtz-Smoluchowski slip velocity [22] condition

$$\mathbf{v}_{\parallel} = -\zeta \mathbf{E}_{\parallel} = -\zeta_w^{eq} \mathbf{E}_{\parallel} - \zeta^i \mathbf{E}_{\parallel}, \quad (7)$$

where the subscript '||' denotes the vector component tangent to the wall. Far upstream and downstream of the corner the pressure and fluid-velocity vector become uniform across the channel. We therefore choose to present the velocity field as the sum of the linear electro-osmotic flow (EOF) and induced contributions

$$\mathbf{v} = \zeta_w^{eq} \nabla \phi_f + \mathbf{v}_{ICEO} = \mathbf{v}_{EOF} + \mathbf{v}_{ICEO}. \quad (8)$$

The first term on the right-hand side of (8) is an irrotational field, and based on the local approximation (5) may be written as

$$\begin{aligned} \mathbf{v}_{EOF} &= \zeta_w^{eq} \nabla \phi_f \\ &= \zeta_w^{eq} \left(1 + \left(\frac{h_1}{h_2} \right)^2 \right)^{1/3} \left(\frac{3}{2} \pi r \right)^{-1/3} \left[\cos \left(\frac{2}{3} (\theta + \pi) \right) \hat{\mathbf{r}} - \sin \left(\frac{2}{3} (\theta + \pi) \right) \hat{\boldsymbol{\theta}} \right]. \end{aligned} \quad (9)$$

The induced part of the velocity \mathbf{v}_{ICEO} is derivable from the stream function ψ satisfying the bi-harmonic equation $\nabla^4 \psi = 0$ together with the requirements that $\psi = const.$ on each segment of the boundary of the fluid domain ($A_\infty BC_\infty$ and $D_\infty EF_\infty$ in Fig. 2) and the slip-velocity condition resulting from the second term of (7). To obtain an approximate 'local' expression for ψ in the vicinity of the corner, the plane polar (r, θ) coordinates were employed such that the origin lies at the corner and $\theta = 0$ corresponds to the bisector of the fluid domain (eq. 3.8' in [3]), from which one obtains

$$\mathbf{v}_{ICEO} = \alpha \left(\frac{3}{2}\right)^{3/2} \left\{ \frac{2}{3\pi} \left[1 + \left(\frac{h_1}{h_2}\right)^2 \right] \right\}^{2/3} \cdot \frac{r^{-2/3}}{3} \left[\left(\cos\left(\frac{1}{3}\theta\right) + 5\cos\left(\frac{5}{3}\theta\right)\right) \hat{\mathbf{r}} - \left(\sin\left(\frac{1}{3}\theta\right) + \sin\left(\frac{5}{3}\theta\right)\right) \hat{\boldsymbol{\theta}} \right]. \quad (10)$$

B. Particle equation of motion

In the limit of low particle concentration, particle-particle interactions may be ignored and the governing kinetic equations for immersed particles include only terms related to the hydrodynamics of the fluid and externally applied forces acting on individual particles. The former includes the ICEO flow and linear EOF, the latter comprised of the DEP and linear electrophoretic (EP) contribution. For a spherical neutrally buoyant particle located at $x_p(t)$ and moving with velocity $\mathbf{v}_p(t)$ within a fluid flow \mathbf{u} , the dimensionless equation of motion has the form [23]

$$St \frac{d\mathbf{v}_p}{dt} = St \frac{\rho_f}{\rho_p} \frac{D\mathbf{u}}{Dt} - St \frac{\rho_f}{2\rho_p} \left[\frac{d\mathbf{v}_p}{dt} - \frac{D}{Dt} \left(\mathbf{u} + \frac{3Fa}{5} \nabla^2 \mathbf{u} \right) \right] - (\mathbf{v}_p - \mathbf{u} - Fa \nabla^2 \mathbf{u}) - Ba \int_0^t \left[\frac{1}{\sqrt{t-\tau}} \frac{d}{d\tau} (\mathbf{v}_p - \mathbf{u} - Fa \nabla^2 \mathbf{u}) \right] d\tau + \mathbf{U}_{\text{Force}}, \quad (11)$$

where $\mathbf{U}_{\text{Force}}$ is a general term for additional forces that may act on the particle, e.g. DEP and EP forces in our case. The typical order of the particle radius $a \sim O(10^{-6}m)$, the channel length scale $L \sim O(10^{-4}m)$, velocity $U_0 \sim O(10^{-3}m/s)$, particle and fluid densities $\rho_f, \rho_p \sim O(10^3 kg/m^3)$ and the fluid dynamic viscosity $\mu \sim O(10^{-3} Pa \cdot s)$. These result in negligible Stokes $\left(St = \frac{2a^2 \rho_p U_0}{9\mu L} \approx 2 \cdot 10^{-6} \right)$, Faxen $\left(Fa = \frac{a^2}{6L^2} \approx 1.7 \cdot 10^{-5} \right)$, and Basset $\left(Ba = a \sqrt{\frac{\rho_f U_0}{\pi \mu L}} \approx 1.7 \cdot 10^{-3} \right)$ dimensionless numbers. Thus, the particle equation of motion can be reduced to

$$\mathbf{v}_p = \mathbf{v}_{LINEAR} + \mathbf{v}_{ICEO} + \mathbf{v}_{DEP}, \quad (12)$$

wherein the linear component comprises of both EOF and EP terms

$$\mathbf{v}_{LINEAR} = \mathbf{v}_{EOF} + \mathbf{v}_{EP} = (\zeta_w^{eq} - \zeta_p^{eq}) \nabla \phi_f = \zeta^{eq} \nabla \phi_f, \quad (13)$$

with the subscripts w and p standing for the microchannel wall and particle, respectively. Since both the microchannel wall and particle surface are negatively charged the EOF and EP counteracts each other with the former being dominant (see section IV.E and Fig 3). To account for particle trapping a non-divergence free attractive force term must be added

[24] which, as was recently shown for the same tracer particles used in the current study [16, 25], is provided by the short-range positive DEP attractive force existing under DC field conditions. The dimensional (symbolized by tilda) dielectrophoretic particle velocity contribution is

$$\tilde{\mathbf{v}}_{DEP} = \frac{\tilde{\mathbf{F}}_{DEP}}{6\pi\eta a} = \frac{\varepsilon_0\varepsilon_f a^2 f_{CM} \tilde{\nabla} |\tilde{\mathbf{E}}|^2}{3\eta}, \quad (14)$$

wherein a is the particle radius and f_{CM} is the Clausius-Mossotti factor [26]. Non-dimensionalization yields

$$\mathbf{v}_{DEP} = \frac{1}{3} f_{CM} \left(\frac{a}{h_1} \right)^2 \nabla |\mathbf{E}|^2, \quad (15)$$

where from the local approximation of the bulk fluid potential (5)

$$\mathbf{v}_{DEP} = -f_{CM} \left(\frac{a}{h_1} \right)^2 \frac{\pi}{3} \left[1 + \left(\frac{h_1}{h_2} \right)^2 \right]^{2/3} \left(\frac{3\pi r}{2} \right)^{-5/3} \hat{\mathbf{r}}. \quad (16)$$

Thus, the total particle velocity (12) can be rewritten in terms of the *relative* contributions of the above linear (9,13), induced (10) and dielectrophoretic(16) velocities,

$$\frac{\mathbf{v}_p}{\zeta^{eq}} = \nabla\phi_f + \lambda_{ICEO} \frac{\mathbf{v}_{ICEO}}{\alpha} + \lambda_{DEP} \frac{\mathbf{v}_{DEP}}{f_{CM} (a/h_1)^2}, \quad (17)$$

where $\lambda_{ICEO} = |\alpha/\zeta^{eq}|$ represents the relative importance of the “induced” and “linear” respective parts of \mathbf{v}_p , while $\lambda_{DEP} = \left| \left(\frac{a}{h_1} \right)^2 f_{CM}/\zeta^{eq} \right|$ represents the relative importance of its “dielectrophoretic” and “linear” respective parts.

IV. RESULTS AND DISCUSSION

A. Experimental

The time evolution of the particle trapping is quantified in Fig. 3 by determining the overall fluorescent intensity within a constant control volume for various applied electric fields ($E_0 < 0$) and particle sizes. The particle net motion away from the corner is in the direction of the electric field indicating the dominance of EOF over EP. Images were obtained using the confocal microscope system. It is clearly demonstrated, based on the slope of the

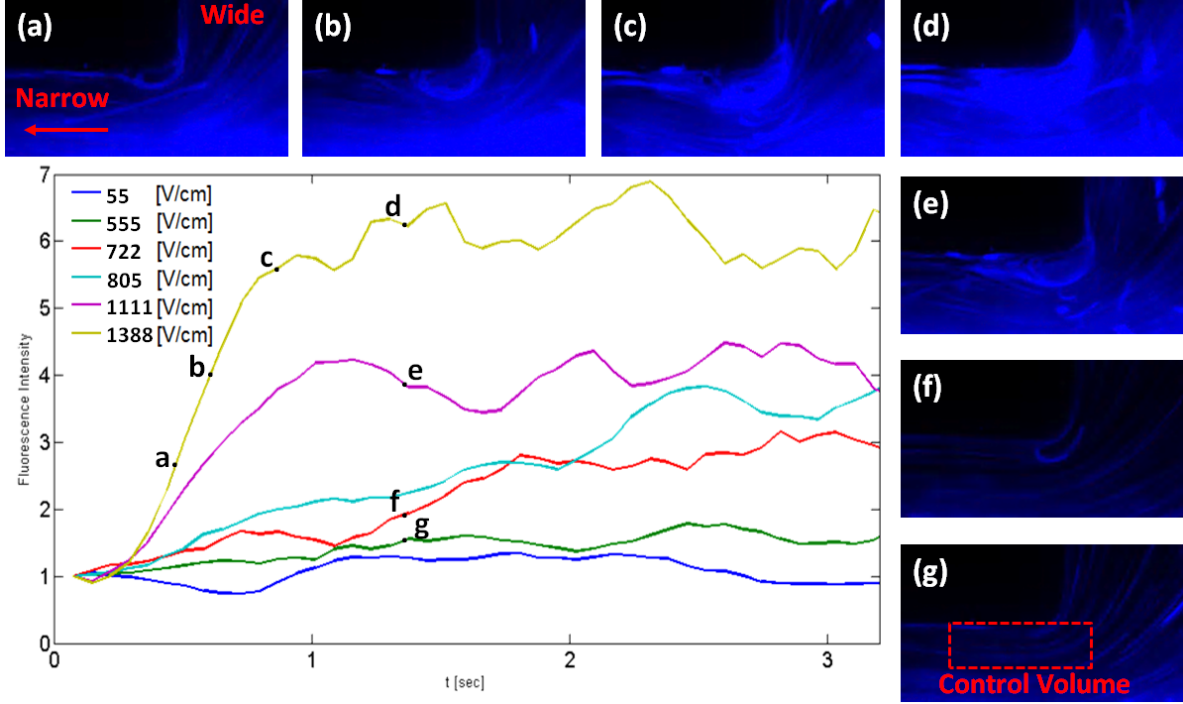


Figure 3: Time evolution of the total fluorescent intensity (normalized by that corresponding to $t=0$ [s]) within the control volume (depicted in inset g) obtained using Confocal microscopy for blue $1[\mu\text{m}]$ fluorescent particles with $\frac{h_2}{h_1} = 5$. Insets a-d are confocal images taken at varying time under a constant applied field of 1388 [V/cm], while insets d-g correspond to a constant time of ~ 1.3 [s] at various applied fields. The arrow in inset a of the figure indicate the direction of the electric field (i.e. $E_0 < 0$) and the net particle motion away from the corner.

curves in Fig. 3, that the accumulation becomes more rapid as the voltage increases. Also, it is seen that for low enough fields (e.g. under ~ 555 [V/cm]) the accumulation is almost negligible. This observation is in qualitative agreement with (15) where it can be seen that the DEP trapping force scales non-linearly with the electric field. The insets a-g in Fig. 3 are confocal images taken at discrete times and various voltages to illustrate the particle accumulation at the corner vicinity assisted by an ICEO vortex downstream of the corner. Insets a-d, corresponding to a constant applied field of 1388 [V/cm], depict the time accumulation of the particles until a saturation like behavior occurs (at ~ 1.3 [s]) which may correspond to a finite capacity of trapped particles (see Movie#1 in [27]). Insets d-g are images taken at time of ~ 1.3 [s], which depict the downstream vortex patterns and particle accumulation for various applied fields. It is clear from Fig. 3 that saturation is reached

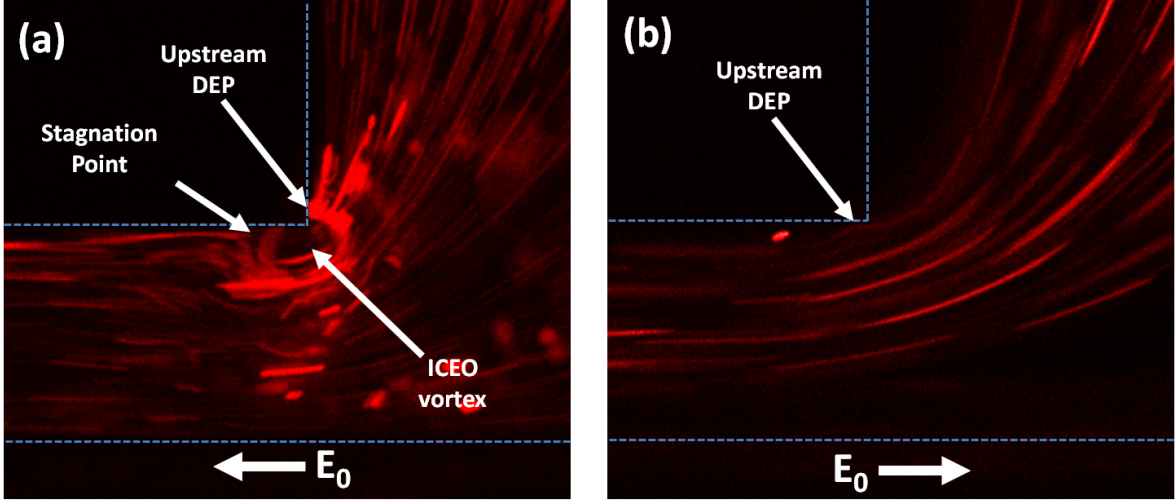


Figure 4: Particle dynamics of fluorescent red $1[\mu\text{m}]$ particles upon reversal of the electric field polarity (bold arrow). $\frac{h_2}{h_1} = 5$, externally applied field $|E_0|$ is $833 [\text{V}/\text{cm}]$.

at longer times with decreased applied fields as can be expected from the corresponding observed decrease in vortex intensities along with particle trapping (insets d-g).

Curiously, upon reversal of the electric field direction, a pronounced asymmetry of the downstream ICEO vortex together with particle trapping (Fig. 4) are observed. For an electric field directed from the narrow to wide channel ($E_0 > 0$) no trapping is seen downstream of the corner and the dark region presumably consists of the downstream vortex (see Movie#2 in [27]). As will be shown theoretically below, for $E_0 > 0$, DEP is no longer effective at trapping particles downstream of the corner. However, upstream of the corner, DEP trapping is observed irrespective of field direction. That the trapping increases with the particle size (Fig. 5) is yet another indication that the mechanism is DEP controlled as the force scales linearly with the particle volume (14) (see Movie #3 in [27]). In the above figures the electric fields within the narrow channels were calculated based on the geometry of the two channels and the applied voltage according to a simplified Ohmic model $E_0 = V/(L(1 + h_1/h_2))$. L is the length of the narrow and wide channels (i.e. 15mm) and V is the applied potential difference across the reservoirs.

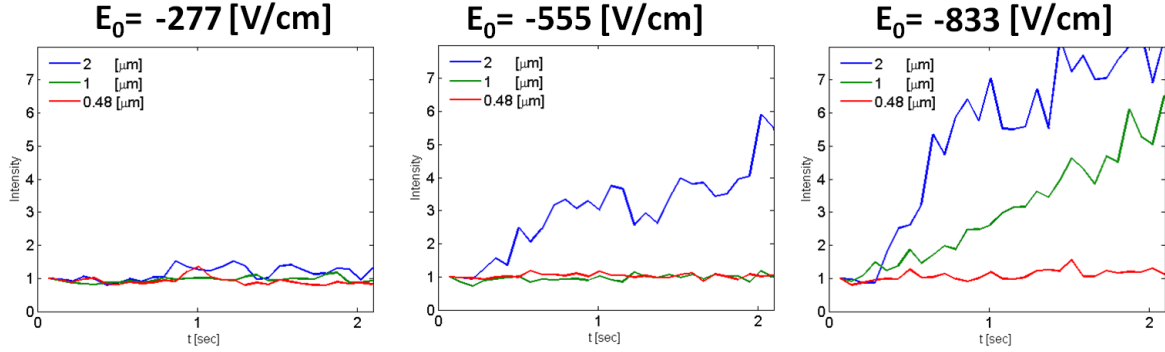


Figure 5: The effect of the particle size on time evolution of the total fluorescent intensity (normalized by that corresponding to $t=0$ [s]) at various applied electric fields.

B. Theoretical model

We examine the evolution of the topology of the particle pathlines in the vicinity of the channel corner for varying ratios $\lambda_{ICEO} = |\alpha/\zeta^{eq}|$ and $\lambda_{DEP} = \left| \left(\frac{a}{h_1} \right)^2 f_{CM}/\zeta^{eq} \right|$. Alternatively, by the assumed scaling of ζ^{eq} , the following also corresponds to the development of the flow and particle dynamics with increasing intensity of the external field. Fig. 6 presents the local particle pathline pattern in the vicinity of the corner (i.e., $r \ll 1$) for $\frac{h_2}{h_1} = 5$ at the indicated values of λ_{ICEO} and λ_{DEP} . Qualitatively similar figures are obtained when selecting other values of $\frac{h_2}{h_1}$. Inset (a) depicts the irrotational antisymmetric velocity field (see the first term in (17)) corresponding to the linear part of \mathbf{v}_p ($\lambda_{ICEO} = 0$, $\lambda_{DEP} = 0$), which is derivable from ϕ_f (5) and represents the superposition of EOF and opposing EP. The induced part ($\lambda_{ICEO} \rightarrow \infty$) of the electro-osmotic flow, \mathbf{v}_{ICEO} , is presented in part (b). The symmetric field obtained from (10) demonstrates the formation of a jet by the convergent flow at the corner. Inset (d) of the same figure shows the flow resulting from the superposition of both the linear and induced flow components for $\lambda_{ICEO} = 0.25$. As $r \rightarrow 0$ the induced velocity ($\propto r^{-2/3}$) prevails over the linear ($\propto r^{-1/3}$) part. Accordingly, it produces a reverse flow along the wall immediately downstream of the corner. This is expected to create a domain of closed streamlines as indeed appears in Fig. 6(d). The extent of this domain is diminishing with decreasing λ_{ICEO} , or equivalently with decreasing electric field intensity, which is in qualitative agreement with the experimental results shown in insets (d-g) of Fig. 3. Upstream of the corner, the superposed velocities accumulate and for this reason no reverse flow appears at the wall. As shown in the sequel, reverse flow and

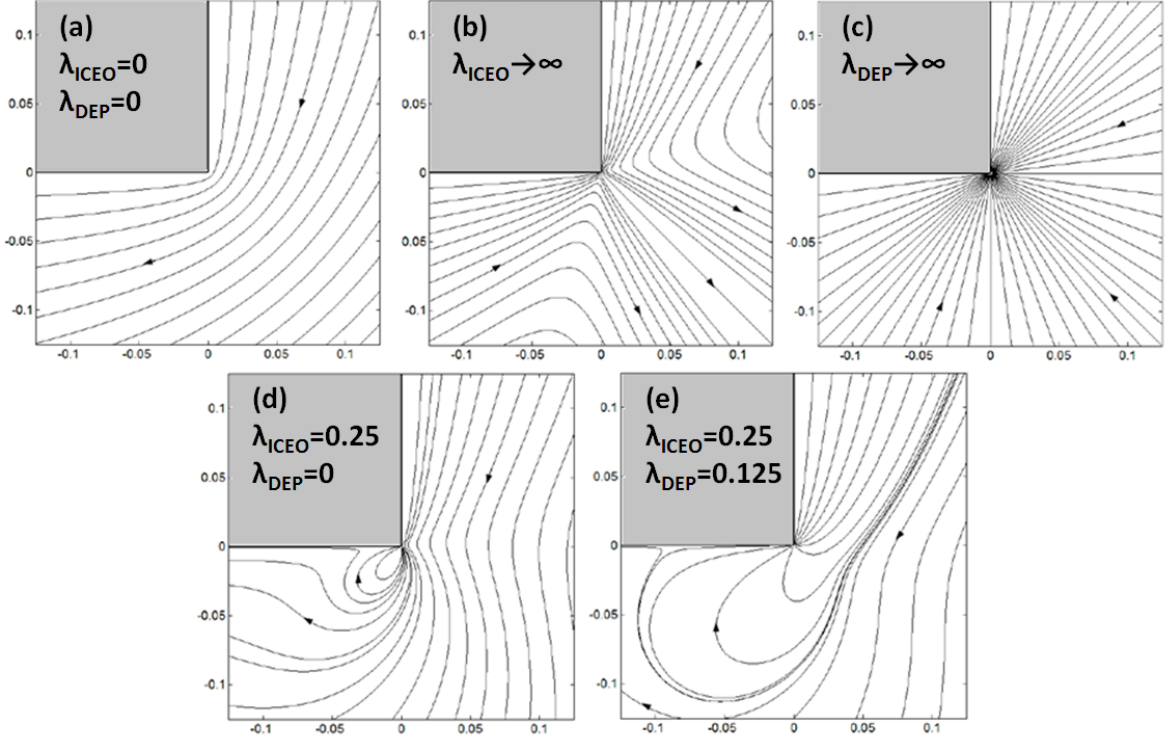


Figure 6: Analytically derivable local flow streamlines (insets (a), (b) and (d)) and particle pathline patterns (insets (c) and (e)) in the vicinity of the corner for $\frac{h_2}{h_1} = 5$, $E_0 < 0$, and the indicated values of λ_{ICEO} and λ_{DEP} .

closed-streamline domains may nevertheless occur upstream of the corner (Fig. 8(a,c) and Yossifon et al. 2006 [3]) for sufficiently large values of λ_{ICEO} . However, unlike the vortex occurring downstream of the corner, this reverse flow occurs near the opposite channel walls ($D_\infty EF_\infty$) and is therefore not a “local” phenomenon. Inset (c) represents the motion of the particles dominated solely by DEP ($\lambda_{DEP} \rightarrow \infty$) whereby the colloids are attracted radially towards the corner acting as a sink. Finally, the particle pathlines resulting from the superposition of the dielectrophoretic contribution ($\lambda_{DEP} = 0.125$) to the ICEO fluid flow ($\lambda_{ICEO} = 0.25$) are shown in inset (e). Here, as $r \rightarrow 0$ it is the DEP velocity that prevails ($\propto r^{-5/3}$) over both the induced ($\propto r^{-2/3}$) and linear ($\propto r^{-1/3}$) velocity components. This manifests itself in attracting pathlines which are downstream towards the corner where particles are trapped. Additionally, the DEP force “breaks” the closed streamlines obtained for the ICEO flow (inset (d)) at the downstream side of the corner. This results in significant enhancement to the trapping rate due to particles arriving from the upstream side. This

prediction is in agreement with the experimental results shown in Figs. 3,4 which illustrate the DEP trapping of the particles both at the upstream side of the corner to which particles pathlines are attracted and at its downstream side where rapid accumulation of particles is assisted by the ICEO vortex. The linear relationship between DEP force and particle volume (16) is clearly visible in the experimental results (Fig. 5) wherein the rate of accumulation increases with increasing particle size.

C. Asymmetry of the problem

An intriguing feature of the experimental results is the distinct difference in particle dynamics and their eventual accumulation upon reversal of the electric field polarity (see Fig. 4). The theoretical predictions based on the approximate 'local' expression of the potential (5); Fig. 6), which is symmetric with respect to θ , cannot account for this effect which stems from the geometrical asymmetry of the L-junction microchannels width $\left(\frac{h_2}{h_1} \neq 1\right)$. In contrast, eqs.(2-4) are the 'global' solution of the potential from which the linear asymmetric particle velocity field can be directly extracted to obtain

$$\mathbf{v}_{LINEAR} = \zeta^{eq} \nabla \phi_f = -\zeta^{eq} \frac{1}{\pi} Re \left\{ \frac{1}{\omega - 1} \frac{d\omega}{dt} \frac{dt}{dz} \nabla z \right\}, \quad (18a)$$

which from equations (2,3) yields

$$\mathbf{v}_{LINEAR} = \zeta^{eq} \frac{h_1}{h_2} [Re \{it\} \hat{\mathbf{x}} - Re \{t\} \hat{\mathbf{y}}]. \quad (18b)$$

We combine this asymmetric linear field (18b) with the induced (10) and DEP (16) velocities in their symmetric form as they decay more rapidly than the linear part ($\propto r^{-5/3}$ and $\propto r^{-2/3}$, as opposed to $\propto r^{-1/3}$ respectively). These combined fields were then calculated in the vicinity of the corner for both polarities of the electric field and are illustrated in Fig. 7. From Fig. 7 it is seen that qualitatively, the DEP trapping mechanism is similar to that described in the symmetric case (Fig. 6(e)), except that when the field is directed from the narrow to wide channels (Fig. 7(b)) the resulting downstream vortex is larger and so is the region of particle pathlines downstream of the corner that terminate at the corner tip (Fig. 7(d)). It is hard to explain based only on this why there is such a distinct difference in the particle entrapment in Fig. 4. However, it is clear that the enlargement of the downstream vortex size in the wider channel compared to that in the opposite direction, due to the

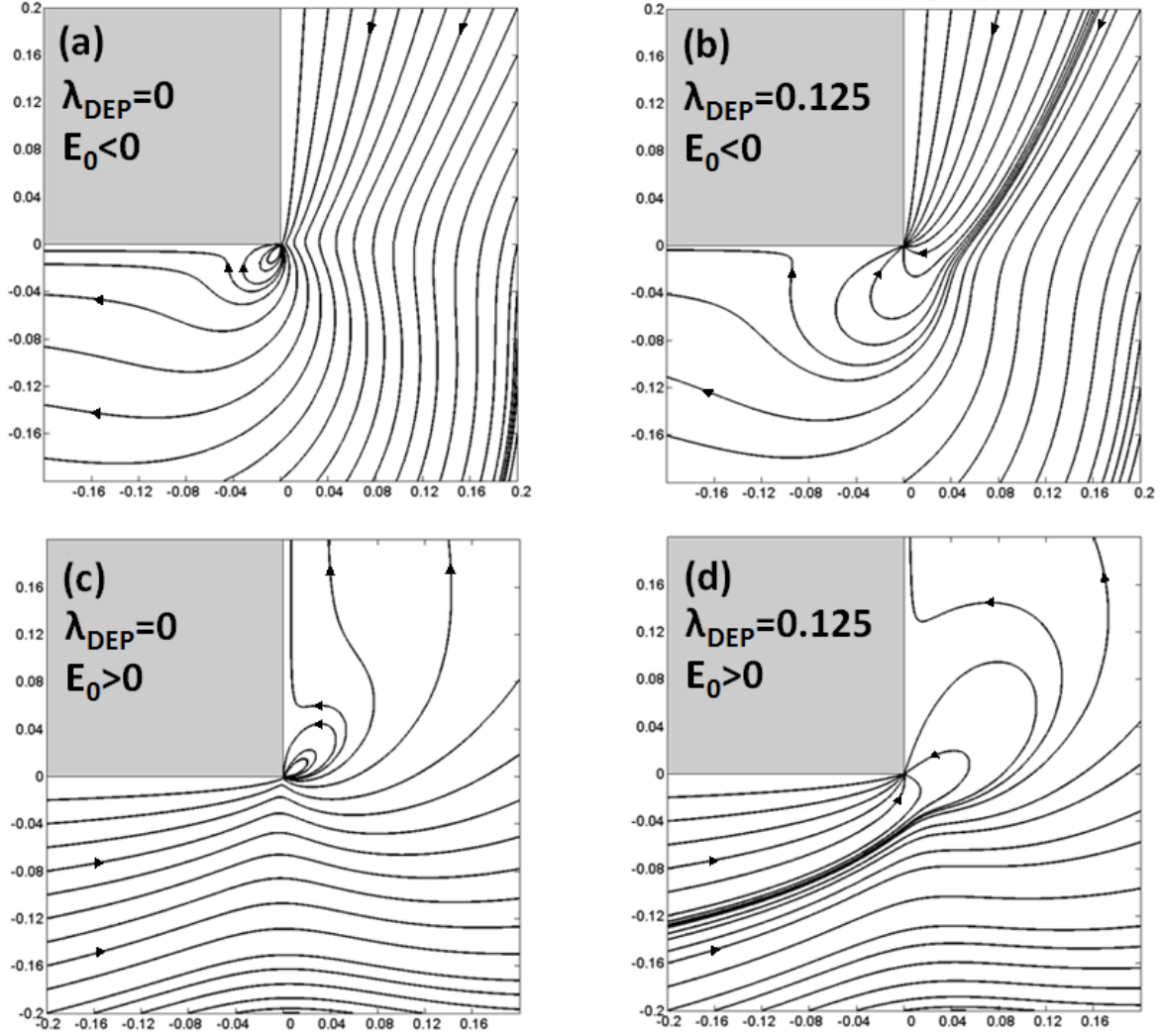


Figure 7: Particle pathlines upon reversal of the applied electric field polarity following an asymmetric linear field with symmetric DEP and ICEO fields, in the vicinity of the corner for $\frac{h_2}{h_1} = 5$ and $\lambda_{ICEO} = 0.25$. The narrow channel is on the bottom-left while the wide channel is on the top-right (see Fig. 2).

asymmetric linear velocity field, occurs concurrently with the decrease of the DEP force due to the same asymmetry of the electric field. With further increase of the electric field, a 'global' solution accounting for the finite dimensions of the channel's width would further emphasize this asymmetry, as will be shown in Fig. 8, where the size of the vortex in the narrow channel is shown to quickly approach its maximum size which is dictated by the channel width.

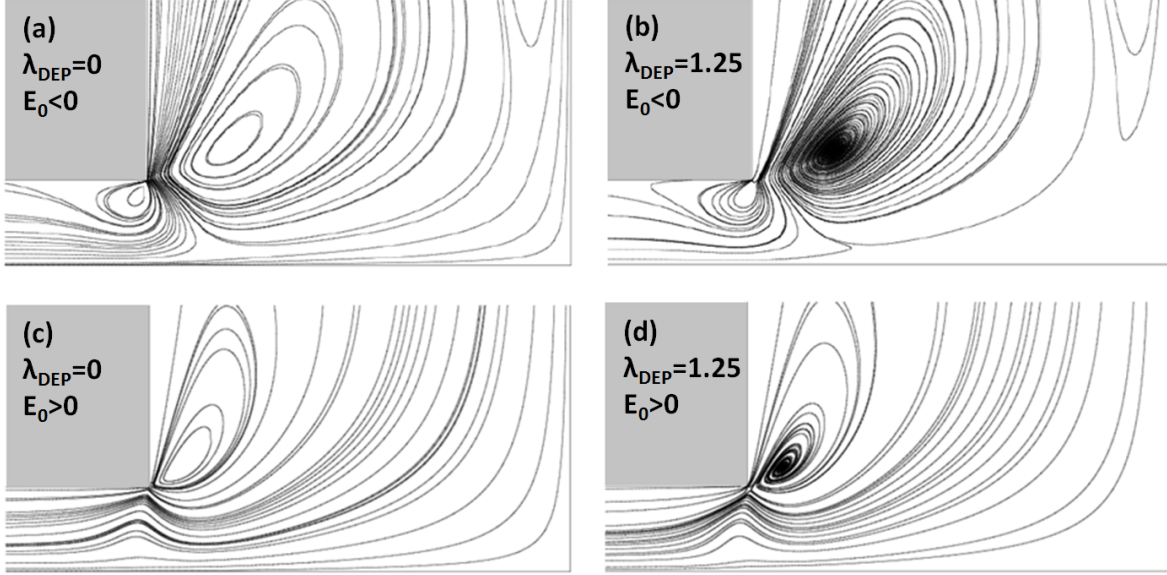


Figure 8: “Global” numerical solution of the particle pathlines patterns upon reversal of the applied electric field polarity for $\frac{h_2}{h_1} = 5$ and $\lambda_{ICEO} = 2.5$,

D. Numerical results

Using commercial code (COMSOL) the decoupled electrostatic (Laplace equations within the bulk fluid and wall domains along with (1)) and hydrodynamic (Stokes and continuity equations along with (7)) equations were solved within the full microchannel domain) rather than only at the very vicinity of the corner as in the analytically derived eqs. (9,10,16). Upon this solution, the particle DEP velocity component (15) was added in order to obtain the particle streamlines. Fig. 8 provides a “global” description of the streamline pattern for $\lambda_{ICEO} = 2.5$ for two opposite electric field polarities with/without the DEP contribution. insets (a) and (c) of the figure show the vortex formation downstream of the corner due to the combined induced and linear flows under reverse field polarity. While the induced ejection intensity is the same in both cases, the linear flows (and the electric fields) roughly differ by a factor of $\frac{h_2}{h_1}$, which corresponds to the ratio of the average velocities within the narrow and wide channels away from the corner, affecting the size of the formed downstream vortex.

Insets (b) and (d) of the figure show the particle pathlines corresponding to the flow fields in insets (a) and (c), respectively, with the addition of the DEP force. That DEP force attracts particles towards the corner is clearly seen both in the upstream side where

streamlines are terminated at the corner and the downstream side where the streamlines (insets (b) and (d)) are also terminated at the corner after converging along the corner wall. These simulation results are in good agreement with both the theoretical (Fig. 6, Fig. 7) results, as well as experimental observations (Fig. 4). Interestingly, upon reversal of the field polarity (inset (d)) the particle streamlines look very different to those in inset (b). This stands in contrast to the analytically predicted asymmetric plot (Fig. 7), where although the size of the downstream vortex was different in correspondence with the channel width, the same qualitative behavior of particle trapping was predicted. This discrepancy can be explained by the fact that the results shown in Fig. 8 were calculated for relative high applied fields wherein the 'global' solution was strongly influenced by the "far" boundaries. In contrast, despite the global linear contribution, the analytical solution remains local (Fig. 7) due to the DEP and ICEO local approximations. This was confirmed by numerical simulations at low enough voltages (Fig. S1 in [27]) which approximate the local solution of Fig. 7.

With the inclusion of the DEP force, the vortex center points (both upstream and downstream) become unstable. In insets (a),(c) the vortices have closed stream/pathlines, as opposed to (b),(d) where particles are moving in a spiral path into/away from the vortex center. This break in the stability of the fixed points is due to the attracting p-DEP force at the corner which leads to their conformation change from closed streamlines to unstable spirals that eject particles from the vortex center. The above arguments support the experimental findings (Fig. 4) where particles were not observed to be trapped upstream of the corner in the case of the field pointing from the narrow to wide channels (i.e. $E_0 > 0$), in contrast to the immense trapping occurring in the opposite direction.

Inset (c) here resembles Fig. 4(c) in [3] in the sense that an upstream vortex may develop, except that the same flow pattern occurs at yet larger λ_{ICEO} values (or equivalently larger electric fields). The difference in the $D_\infty E$ (bottom) boundary condition (H-S slip condition at the wall instead of a symmetry line) delays the flow reversal within the narrow channel upstream of the corner, resulting from the continuity of the mass flow rate, which is necessary for obtaining the downstream vortex.

E. Scaling arguments regarding the different competing mechanisms

Here we use the following quantities: $\epsilon_0 = 8.85 \cdot 10^{-12} \text{F/m}$ is the vacuum permittivity; $\epsilon_f = 80$ and $\epsilon_w = 3$ are the relative dielectric constants of the fluid and microchannel (PDMS), respectively; $R = 8.314 \text{J/(K}\cdot\text{mol)}$ is the universal gas constant; $T = 300 \text{K}$ is the absolute temperature; $F = 9.648 \cdot 10^4 \text{C/mol}$ is the Faraday constant; $c_0 = 10^{-5} \text{M}$ is the bulk ionic concentration; $h_1 = 80 \cdot 10^{-6} \text{m}$ is the narrow channel width; $a = 0.5 \cdot 10^{-6} \text{m}$ is the particle radius; $\sigma_p = 133.5 \mu\text{S/cm}$ (obtained for DI, i.e. $\sigma_f = 0.05 \mu\text{S/cm}$ [25]) and $\sigma_f = 2 \mu\text{S/cm}$ (measured) are the conductivities of the particle (effective conductivity due to surface conduction) and medium; the zeta potential of the PDMS can be estimated as[28] $\tilde{\zeta}_w^{eq} = -50 \text{mV}$ for $\text{pH} \approx 5.5$ (measured) while that of polystyrene particles $\tilde{\zeta}_p^{eq} = -34 \text{mV}$ (measured using Zetasizer for $1 \mu\text{m}$ particles in $3 \cdot 10^{-5} \text{M}$ solution, $\sigma_f = 4 \mu\text{S/cm}$).

Hence, $\kappa^{-1} = \lambda_D = \sqrt{\frac{\epsilon_0 \epsilon_f R T}{2 F^2 c_0}} \approx 97 \text{nm}$ is the Debye length. Using the following expressions: $\alpha = \frac{\epsilon_w \lambda_D}{\epsilon_f h_1}$, $\zeta^{eq} = \frac{\tilde{\zeta}^{eq}}{E_0 h_1}$ (wherein the tilde stands for the dimensional zeta-potential) and $f_{CM} = \frac{\sigma_p - \sigma_f}{\sigma_p + 2\sigma_f} \approx 0.96$ then for a value of $E_0 = 1388 \text{V/cm}$ (corresponding to the case when the combined effect of all competing mechanisms is most clearly seen experimentally in Fig.3):

$$\lambda_{ICEO} = \frac{\alpha}{\zeta^{eq}} = \frac{\alpha}{\zeta_w^{eq} - \zeta_p^{eq}} = \frac{\epsilon_w \lambda_D}{\epsilon_f (\tilde{\zeta}_w^{eq} - \tilde{\zeta}_p^{eq})} E_0 \approx 0.028 \quad (19a)$$

$$\lambda_{DEP} = \left(\frac{a}{h_1} \right)^2 \frac{f_{CM}}{\zeta^{eq}} = \frac{a^2}{h_1} \frac{f_{CM}}{(\tilde{\zeta}_w^{eq} - \tilde{\zeta}_p^{eq})} E_0 \approx 0.023 \quad (19b)$$

Interestingly, the ratio $\lambda_{ICEO}/\lambda_{DEP} \approx 1.21$ is in agreement with the theoretical analysis wherein a ratio of the $O(1)$ was used. These values are smaller by factors of ≈ 9 and ≈ 5 than the theoretical values of $\lambda_{ICEO} = 0.25$ and $\lambda_{DEP} = 0.125$ (Fig.6), corresponding to the case when all competing mechanisms exist simultaneously to obtain qualitatively the combined effect observed experimentally at high applied fields ($E_0 = 1388 \text{V/cm}$). Such a discrepancy is not unexpected in the very crude estimates of scaling analysis. However, one plausible explanation for this could be that while DEP, ICEP and EP are local effects (the former two are non-negligible only at the vicinity of the corner while the latter depends only on the local electric field) the electroosmotic flow must obey the continuity equation (i.e. mass flux balance) everywhere in the system. Thus, it is more prone to disturbances,

.e.g reservoir-microchannel entrance effects inducing back pressure which may lower the net EOF flow, resulting, in better agreement between theory and experiments.

V. CONCLUDING REMARKS

The purpose of the present contribution is to study the colloid dynamics in conjunction with appearance of ICEO vortices in a micro-channel junction configuration. Our main experimental results appear in Fig. 3 where we demonstrate the rapid particle trapping and accumulation at the vicinity of the corner. The exact nature of the interparticle forces [e.g. Posner 2009[29]] existing at the corner vicinity when the particle accumulation becomes significant is beyond the scope of the current study as we are mainly concerned with the physical mechanism that is responsible, in the first place, for the migration of particles towards the corner where they can potentially accumulate. This phenomenon was shown theoretically, at the single particle level, to be due to the combination of a short-range non-divergence free DEP trapping force which is assisted by a far-field electro-convection downstream vortex that feeds the corner with particles (Fig. 6). The analytical model is a local approximation of the global solution in the vicinity of the corner. Accordingly, the resulting expressions involve no indeterminate parameters whose evaluation would require the use of various ad hoc estimates, in particular with respect to obtaining a correct description of the dielectrophoretic contribution to the particle velocity superposed on the ICEO and linear flow velocities. Finally, we clearly demonstrate that the sharp corner geometry, in addition to its potential to greatly enhance forced convection due to the intensified velocity near the channel walls around the induced vortex, can also be used for rapid trapping of colloids.

Acknowledgments

We thank Alicia Boymelgreen for her invaluable inputs. This work was supported by ISF grant 1078/10. The fabrication of the chip was possible through the financial and technical support of the Technion RBNI (Russell Berrie Nanotechnology Institute) and MNFU (Micro

- [1] Paul Takhistov, Ksenia Duginova, and Hsueh-Chia Chang. Electrokinetic mixing vortices due to electrolyte depletion at microchannel junctions. *Journal of Colloid and Interface Science*, 263(1):133–143, July 2003.
- [2] Sunil Kumar Thamida and Hsueh-Chia Chang. Nonlinear electrokinetic ejection and entrainment due to polarization at nearly insulated wedges. *Physics of Fluids*, 14(12):4315–4328, November 2002.
- [3] G. Yossifon, I. Frankel, and T. Miloh. On electro-osmotic flows through microchannel junctions. *Physics of Fluids*, 18(11):117108–117108–9, November 2006.
- [4] Yuval Eckstein, Gilad Yossifon, Avraham Seifert, and Touvia Miloh. Nonlinear electrokinetic phenomena around nearly insulated sharp tips in microflows. *Journal of Colloid and Interface Science*, 338(1):243–249, October 2009.
- [5] Zhemin Wu and Dongqing Li. Micromixing using induced-charge electrokinetic flow. *Electrochimica Acta*, 53(19):5827–5835, August 2008.
- [6] Jia-Kun Chen and Ruey-Jen Yang. Vortex generation in electroosmotic flow passing through sharp corners. *Microfluidics and Nanofluidics*, 5(6):719–725, December 2008.
- [7] Hui Zhao and Haim H. Bau. Microfluidic chaotic stirrer utilizing induced-charge electro-osmosis. *Physical Review E*, 75(6):066217, June 2007.
- [8] Todd M. Squires and Martin Z. Bazant. Induced-charge electro-osmosis. *Journal of Fluid Mechanics*, 509:217–252, June 2004.
- [9] Sarah J. R. Staton, Kang Ping Chen, Thomas J. Taylor, Jose Rafael Pacheco, and Mark A. Hayes. Characterization of particle capture in a sawtooth patterned insulating electrokinetic microfluidic device. *ELECTROPHORESIS*, 31(22):3634–3641, 2010.
- [10] Soumya K. Srivastava, Aytug Gencoglu, and Adrienne R. Minerick. DC insulator dielectrophoretic applications in microdevice technology: a review. *Analytical and Bioanalytical Chemistry*, 399(1):301–321, January 2011.
- [11] Kuo-Tang Liao and Chia-Fu Chou. Nanoscale molecular traps and dams for ultrafast protein enrichment in high-conductivity buffers. *Journal of the American Chemical Society*, 134(21):8742–8745, May 2012.

- [12] A. Ramos, H. Morgan, N. G. Green, and A. Castellanos. Ac electrokinetics: a review of forces in microelectrode structures. *Journal of Physics D: Applied Physics*, 31(18):2338, September 1998.
- [13] Antonio Ramos, Hywel Morgan, Nicolas G Green, and Antonio Castellanos. AC electric-field-induced fluid flow in microelectrodes. *Journal of Colloid and Interface Science*, 217(2):420–422, September 1999.
- [14] Jie Wu, Yuxing Ben, David Battigelli, and Hsueh-Chia Chang. Long-range AC electroosmotic trapping and detection of bioparticles. *Industrial & Engineering Chemistry Research*, 44(8):2815–2822, April 2005.
- [15] Kai F. Hoettges, Martin B. McDonnell, and Michael P. Hughes. Use of combined dielectrophoretic/electrohydrodynamic forces for biosensor enhancement. *Journal of Physics D: Applied Physics*, 36(20):L101, October 2003.
- [16] Yoav Green and Gilad Yossifon. Dynamical trapping of colloids at the stagnation points of electro-osmotic vortices of the second kind. *Physical Review E*, 87(3):033005, March 2013.
- [17] Janelle R. Anderson, Daniel T. Chiu, Rebecca J. Jackman, Oksana Cherniavskaya, J. Cooper McDonald, Hongkai Wu, Sue H. Whitesides, and George M. Whitesides. Fabrication of topologically complex three-dimensional microfluidic systems in PDMS by rapid prototyping. *Analytical Chemistry*, 72(14):3158–3164, July 2000.
- [18] Kathryn Haubert, Tracy Drier, and David Beebe. PDMS bonding by means of a portable, low-cost corona system. *Lab on a Chip*, 6(12):1548–1549, November 2006.
- [19] G. Y. Tang, D. G. Yan, C. Yang, H. Q. Gong, C. J. Chai, and Y. C. Lam. Joule heating and its effects on electroosmotic flow in microfluidic channels. *Journal of Physics: Conference Series*, 34(1):925, April 2006.
- [20] L. D. Landau, L. P. Pitaevskii, and E. M. Lifshitz. *Electrodynamics of Continuous Media, Second Edition: Volume 8*. Butterworth-Heinemann, 2 edition, January 1984.
- [21] L. M. Milne-Thomson and Physics. *Theoretical Hydrodynamics*. Dover Publications, 5 edition, February 2011.
- [22] J. Lyklema. *Fundamentals of Interface and Colloid Science: Solid-Liquid Interfaces*. Academic Press, 1 edition, December 1995.
- [23] Armando Babiano, Julyan H. E. Cartwright, Oreste Piro, and Antonello Provenzale. Dynamics of a small neutrally buoyant sphere in a fluid and targeting in hamiltonian systems. *Physical*

- Review Letters*, 84(25):5764–5767, June 2000.
- [24] Shui-Jin Liu, Hsien-Hung Wei, Shyh-Hong Hwang, and Hsueh-Chia Chang. Dynamic particle trapping, release, and sorting by microvortices on a substrate. *Physical Review E*, 82(2):026308, August 2010.
- [25] Lichen Rozitsky, Amir Fine, Dekel Dado, Shahar Nussbaum-Ben-Shaul, Shulamit Levenberg, and Gilad Yossifon. Quantifying continuous-flow dielectrophoretic trapping of cells and micro-particles on micro-electrode array. *Biomedical Microdevices*, 15(5):859–865, October 2013.
- [26] T. B Jones. *Electromechanics of particles*. Cambridge University Press, Cambridge; New York, 1995.
- [27] Supplementary materials, July 2013.
- [28] Brian J Kirby and Jr Hasselbrink, Ernest F. Zeta potential of microfluidic substrates: 2. data for polymers. *Electrophoresis*, 25(2):203–213, January 2004. PMID: 14743474.
- [29] Jonathan D. Posner. Properties and electrokinetic behavior of non-dilute colloidal suspensions. *Mechanics Research Communications*, 36(1):22–32, January 2009.